Received: 9 August 2024 | Revised: 13 September 2024 | Accepted: 29 September 2024

DOI: 10.1002/elt2.73

RESEARCH ARTICLE

WILEY

Design of long-wavelength infrared InAs/InAsSb type-II superlattice avalanche photodetector with stepped grading layer

Keming Cheng[1] | **Kai Shen**[1] | **Chuang Li**[1,2] | **Daqian Guo**[1] | **Hao Wang**[3] | **Jiang Wu**[1,4]

[1]Institute of Fundamental and Frontier Sciences, University of Electronic Science and Technology of China, Chengdu, China

[2]Intelligent Terminal Key Laboratory of SiChuan Province, Yibin Institute of UESTC, Yibin, China

[3]Division of Electrical Engineering, Department of Engineering, University of Cambridge, Cambridge, UK

[4]State Key Laboratory of Electronic Thin Films and Integrated Devices, University of Electronic Science and Technology of China, Chengdu, China

Correspondence

Kai Shen, Daqian Guo and Jiang Wu.
Email: kaishen@uestc.edu.cn, daqianguo@uestc.edu.cn and jiangwu@uestc.edu.cn

Funding information

Fundamental Research Funds for the Central Universities, Grant/Award Number: ZYGX2019Z018; National Natural Science Foundation of China, Grant/Award Number: 61974014; Innovation Group Project of Sichuan Province, Grant/Award Number: 20CXTD0090

Abstract

Weak response in long-wavelength infrared (LWIR) detection has long been a perennial concern, significantly limiting the reliability of applications. Avalanche photodetectors (APDs) offer excellent responsivity but are plagued by high dark current during the multiplication process. Here, we propose a high-performance type-II superlattices (T2SLs) LWIR APD to address these issues. The low Auger recombination rate of the InAs/InAsSb T2SLs absorption layer is exploited to reduce the dark current initially. AlAsSb with a low k value is employed as the multiplication layer to suppress device noise while maintaining sufficient gain. To facilitate carrier transport, the conduction band discontinuity is optimized by inserting an InAs/AlSb T2SLs stepped grading layer between the absorption and multiplication layers. As a result, the device exhibits excellent photoresponse at 8.4 μm at 100 K and maintains a low dark current density of 5.48×10^{-2} A/cm^2. Specifically, it achieves a maximum gain of 366, a responsivity of 650 A/W, and a quantum efficiency of 26.28% under breakdown voltage. This design offers a promising solution for the advancement of LWIR detection.

KEYWORDS

AlAsSb, avalanche photodetector, InAs/InAsSb type-II superlattice

1 | INTRODUCTION

Long-wavelength infrared (LWIR) detection has been considered as one of the crucial technologies that advances the development of both military and civilian applications, including biomedical engineering, optical ranging, astronomical observation, etc.[1–4] Many of these applications require the operation of infrared systems in low photon flux conditions.[5] However, the high dark current and intrinsic noise

limit the overall performance of the state-of-the-art LWIR detectors, making it challenging to accurately detect low-intensity infrared signals.[6–9] Avalanche photodetectors (APDs) feature high gain, making them one of the promising candidates for low light detection.[10] HgCdTe APDs possess outstanding responses with low excess noise and high gain. Recently, researchers have found that a larger spin-orbit splitting energy can effectively prevent holes from scattering to the separation band, thereby reducing excess noise in the APD.[11] But they are limited by poor compositional uniformity and high fabrication cost, particularly in the LWIR region.[12–14] Therefore, opportunities exist to optimize device structure or explore alternative materials to achieve high-performance LWIR APDs.

Thanks to the emerging type-II superlattices (T2SLs) with low Auger recombination rates and excellent material uniformity, high-performance T2SL LWIR photodetectors have been widely reported.[15–18] Particularly, compared with InAs/GaSb T2SLs, InAs/InAsSb T2SLs offer prolonged carrier lifetimes with the elimination of Ga-related defect states and simplified heterointerface.[19] Meanwhile, only the switch of the Sb valve needs to be controlled using molecular beam epitaxy, which benefits large-scale production with good epitaxial interfacial quality.[20] Noteworthy, due to the low conduction band, the defect state band is located above the conduction band, thus increasing the tolerance to defects and thereby extending the carrier lifetime.[21] These features help reduce the dark current of the APD, thereby improving device response and operating temperature. In addition, to optimize the noise characteristics of APDs and increase the device gain, the multiplication layer (ML) often employs materials with a wide bandgap and low k value (where $k = \alpha/\beta$, α and β are the ionization coefficients of electrons and holes, respectively).[22–25] Lower k values correspond to reduced excess noise in the device, thus further enhancing performance.[26] AlAsSb, with its exceptionally low k value, has garnered attention for this purpose, making it an ideal material for the ML of APD.[27–29] Recently, III-V T2SL-based MWIR APDs have been demonstrated,[30] yet developing LWIR T2SL APDs remains challenging.

In this study, a long-wavelength infrared APD featuring an InAs/InAsSb T2SLs absorption layer (AL) is proposed. To address the conduction band discontinuity between InAs/InAsSb T2SLs and AlAsSb, an InAs/AlSb T2SLs stepped grading layer is designed to facilitate carrier transport. As a result, through simulation, we achieved a high-performance LWIR T2SL APD with a peak wavelength of 8.4 μm. At 100 K, the device exhibits a maximum gain of 366 with a corresponding responsivity of 650 A/W and a quantum efficiency (QE) of 26.28%.

2 | RESULTS AND DISCUSSION

2.1 | Design of T2SL and device structures

Determining the composition and thickness of InAs/InAsSb T2SLs is crucial, with adjustments made to achieve stress balance. In the context of LWIR detection, a thicker single period of InAs/InAsSb T2SLs is necessary to attain the same cutoff wavelength as InAs/GaSb T2SLs. However, thicker single period result in reduced absorption coefficients and increased effective mass of holes in the growth direction within T2SLs. Ting et al.[3] discovered experimentally that increasing the Sb component enables achieving a longer cutoff wavelength without significantly increasing the single period thickness. However, an excessively high Sb component risks Sb element segregation.[31,32] Consequently, InAs/$InAs_{0.5}Sb_{0.5}$ T2SLs, with an Sb component of 0.5, are chosen as the AL for the APD.

InAs/InAsSb T2SLs are predominantly grown on GaSb substrates, necessitating consideration of GaSb's role in strain management. In essence, achieving strain balance involves comparing the average lattice constant of one period of the superlattice with that of the substrate.[33] Typically, the tensile strain in InAs is compensated by the compressive strain introduced by InAsSb, resulting in a thicker InAs layer compared to InAsSb. Therefore, the thickness of each layer in InAs/InAsSb T2SLs can be calculated using the following formula:

$$t_{\mathrm{InAsSb}} = \left(\frac{a_{\mathrm{GaSb}} - a_{\mathrm{InAs}}}{a_{\mathrm{InSb}} - a_{\mathrm{InAs}}}\right) \cdot \left(\frac{P}{x_{\mathrm{Sb}}}\right) \approx 0.090 \cdot \left(\frac{P}{x_{\mathrm{Sb}}}\right) \quad (1)$$

where t_{InAs} and t_{InAsSb} represent the thickness of InAs and InAsSb materials in one period, respectively. P represents the total thickness of a single period of the superlattice, x_{Sb} represents the composition of Sb, and a represents the lattice constant of each material.[34] The ratio of single atomic layers between InAs and $InAs_{0.5}Sb_{0.5}$ in one period is determined as approximately 4:1. With this ratio, InAs/$InAs_{0.5}Sb_{0.5}$ T2SLs achieves strain balance, mitigating the significant dislocations or defects during epitaxial growth. The key material parameters of InAs/$InAs_{0.5}Sb_{0.5}$ T2SLs are listed in Table 1.[35–40] Figure 1A,B show the band structure and absorption coefficient of 32 monolayers InAs/$InAs_{0.5}Sb_{0.5}$, respectively. The effective bandgap of 25.6 monolayers InAs/6.4 monolayers $InAs_{0.5}Sb_{0.5}$ T2SLs is calculated as 132 meV at 150 K, corresponding to a 50% cut-off wavelength of 9.4 μm, and it reaches a peak absorption of about 2200 cm^{-1} around 8.4 μm.

The schematic of the InAs/$InAs_{0.5}Sb_{0.5}$ long-wavelength infrared APD structure is illustrated in

TABLE 1 Material parameters used in InAs/InAsSb T2SLs modeling.[35–40]

Parameters	Symbol (unit)	InAs	InSb	GaSb
Bandgap $E_g(T) = E_g(T = 0\ \mathrm{K}) - \frac{\alpha T^2}{T+\beta}$	α (meV/K)	0.276	0.32	0.417
	β (K)	93	170	140
	E_g ($T = 0$ K) (eV)	0.417	0.25	0.812
Minority carrier lifetime	τ (ns)	325	300	100
Luttinger parameters	γ_1	20.0	34.8	13.4
	γ_2	8.5	15.5	4.7
	γ_3	9.2	16.5	6
Imaginary refractive index	k	0.001	0.0082	0.01
Elastic constant	C_{11} (GPa)	832.9	684.7	884.2
	C_{22} (GPa)	452.6	373.5	402.6
	C_{44} (GPa)	395.9	311.1	432.2
Spin-orbit energy	Δ_0 (eV)	0.39	0.82	0.76
Kane potential	E_p (eV)	21.5	24.08	24.76
Effective mass (0 K)	$\frac{m_e^*}{m_0}$	0.023	0.0138	0.038

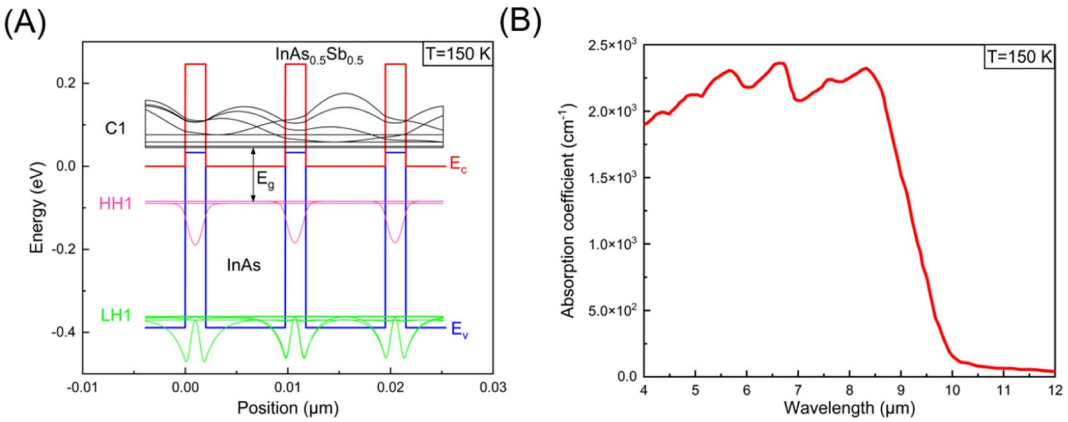

FIGURE 1 (A) Energy band structure of InAs/$InAs_{0.5}Sb_{0.5}$ T2SLs with a single period of 32 monolayers. He red line represents the conduction band, the blue line represents the valence band, the black line represents the conduction band (C1) microstrip, the pink line represents the heavy hole (HH1) microstrip, and the green line represents the light hole (LH1) microstrip. (B) Absorption spectrum of 32 monolayers InAs/$InAs_{0.5}Sb_{0.5}$ T2SLs.

Figure 2A. The structure from bottom to top is as follows: a GaSb substrate, a 50 nm thick GaSb buffer layer that enhances lattice matching and reduces interface defect density, a 100 nm thick n-type heavily doped (1×10^{18} cm^{-3}) GaSb bottom contact layer, and subsequently, a 400 nm thick unintentionally doped $AlAs_{0.09}Sb_{0.91}$ ML to leverage its low k value and broad bandgap, thus effectively minimizing device noise. Then a 50 nm thick AlAsSb charge layer with a doping concentration of 1×10^{16} cm^{-3} was designed to adjust the electric field between the AL and ML, a 64 nm thick InAs/AlSb T2SLs was designed to facilitate carrier transport. Next, a 1100 nm thick p-type doped InAs (77.5 Å)/$InAs_{0.5}Sb_{0.5}$ (20 Å) T2SLs AL of 3×10^{14} cm^{-3} was designed. Finally, a 100 nm thick InAs/$InAs_{0.5}Sb_{0.5}$ (p-type, 5×10^{18} cm^{-3}) T2SLs top contact layer was designed to form ohmic contact. The stepped grading layer is a 14-level structure with InAs/AlSb T2SLs as: 80/10, 60/24, 40/24, 30/24, 24/24, 18/24, 15/24, 12/24, 10/24, 8/24, 6/24, 4/24, 3/24 and 2/30, in a unit of Å. When reverse biased, a strong electric field is formed in the ML of the device to achieve impact ionization. Moreover, the ML not only aids in carrier transport but also, through doping, helps confine the electric field within the AL.[30] This ensures that while the electric field in the AL fosters carrier transport, it does not induce tunneling,[41,42] which can be seen from the device electric field schematic diagram shown in Figure 2B. Figure 3 shows the band structure of the device when the

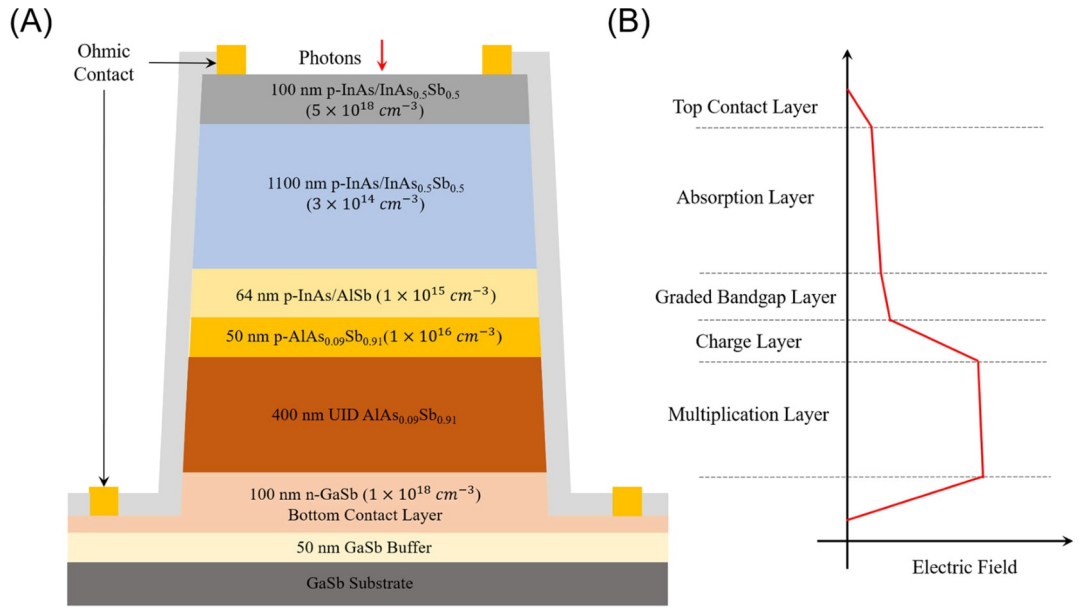

FIGURE 2 (A) The diagram of InAs/InAsSb long-wavelength infrared APD. (B) The diagram of the electric field of each layer in APD. APD, avalanche photodetector.

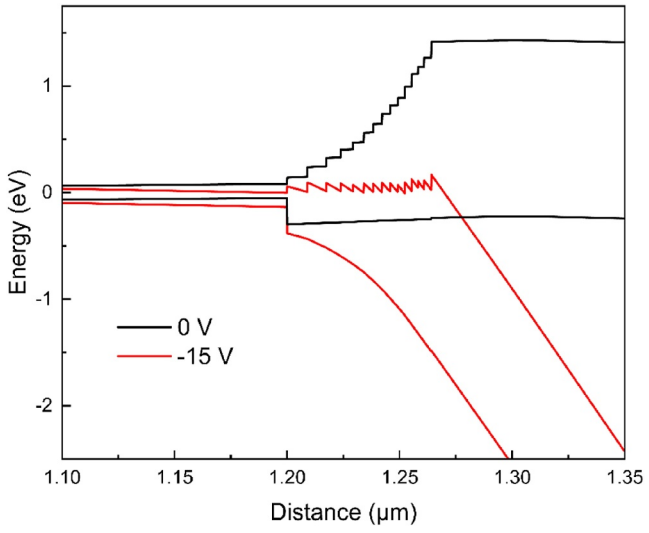

FIGURE 3 The simulation result of the energy band structure of the APD at the interface of the absorption layer/stepped grading layer/charge layer/multiplication layer at thermal equilibrium and −15 V external bias. APD, avalanche photodetector.

reverse bias is 0 V and −15 V, respectively. The simulation shows that at −15 V, the average electric fields in the AL and ML are approximately 5 kV/cm and 300 kV/cm, respectively.

2.2 | The photoresponse of the APD

Figure 4A shows the temperature-dependent dark current characteristics of InAs/InAsSb LWIR APD. The dark current density (J_d) increases rapidly with the elevated operating temperature. Below −5 V bias voltage, at lower temperatures, the J_d remains relatively constant as thermal excitation of carriers is minimal, impeded by the significant conduction band difference. As temperature increases, carrier thermal excitation intensifies, allowing a small fraction of hot carriers to surmount the barrier and contribute to the current. With the voltage surpassing −5 V, the electric field extends beyond the ML to the stepped grading layer, flattening the energy band and facilitating carrier transport, thereby amplifying the dark current. Upon reaching a voltage of approximately −15 V, carrier transport saturates, and the J_d plateaus. When the voltage further increases to about −41.2 V, the electric field of the ML becomes large enough to satisfy the carrier collision ionization process and trigger avalanche, resulting in a rapid increase in J_d.

At 100 K, the punch-through voltage (V_{pt}) of this APD is −15 V. Beyond this threshold, part of the voltage falls on the AL, and at the breakdown voltage (V_{bd}) of −41.2 V, the device exhibits significant gain. Notably, as depicted by the black arrow in Figure 4A, the V_{bd} of the APD increases with rising operating temperatures. When a large voltage is applied, the avalanche breakdown process usually exhibits a positive temperature coefficient. In order to overcome the increased carrier cooling caused by phonon scattering, a higher applied voltage is required to achieve breakdown.[43] The J_d of the device is finally calculated at 100 K and 95% breakdown voltage to be 5.48×10^{-2} A/cm^2. In the actual growth and preparation process, surface leakage current will be an important factor affecting the

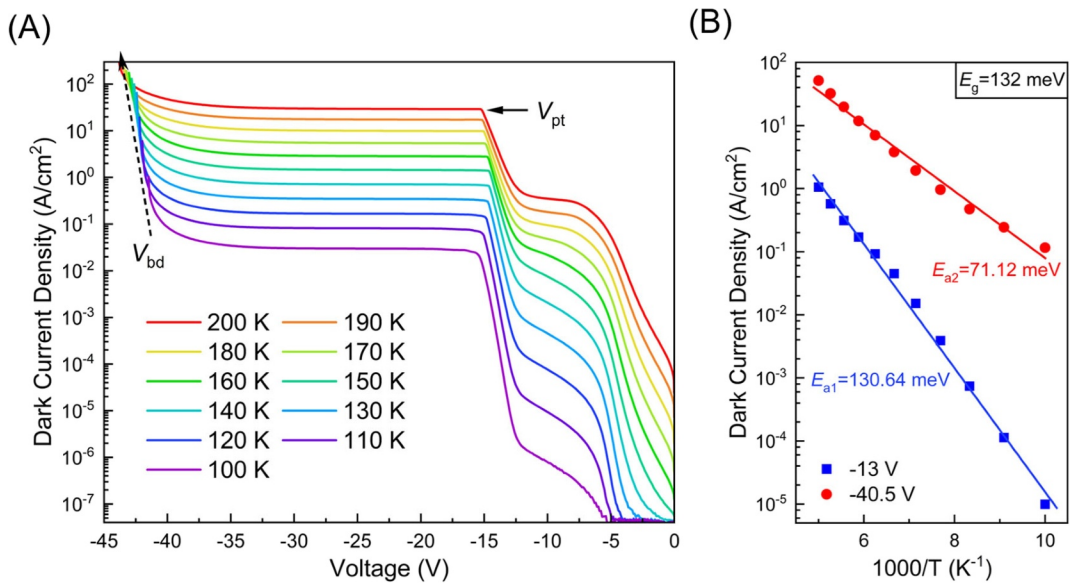

FIGURE 4 (A) J_d of APD as a function of voltage at different temperatures. (B) Arrhenius curves of the J_d of the APD under voltages of −13 V (before punch-through) and −40.5 V (before breakdown). The points are the simulation results and the lines are the fitting curves. APD, avalanche photodetector.

APD performance. In the actual growth process, surface leakage current will reduce the breakdown voltage stability of the device, leading to premature breakdown and unreliable gain control. To address this issue, several mitigation strategies can be adopted. Improving manufacturing accuracy[44,45] and adding passivation layers[46] (such as SU8 or Al_2O_3[47]) after preparation will help reduce surface states. In addition, optimizing device design such as adding guard rings[14] around the edges can effectively locate and reduce surface leakage current. Through the above measures, APDs can achieve higher efficiency, lower noise and more consistent operation, which is critical for the future development of applications, such as optical communications, imaging, and LiDAR systems.

Figure 4B shows the corresponding Arrhenius curves of the J_d of the APD at −13 V (before punch-through) and −40.5 V (before breakdown). By fitting the temperature-dependent current data, the activation energy (E_a) of the APD can be calculated by formulas: $J_{diff} \propto T^3 \exp(-E_a/k_bT)$ and $J_{G-R} \propto T^{3/2} \exp(-E_a/2k_bT)$, where J_{diff} is the diffusion current density and J_{G-R} is the generation-recombination (G-R) current density.[48–50] When applying a bias of −13 V, E_a is calculated as 130.64 meV, which closely aligns with the bandgap energy (132 meV) of 32 monolayers InAs/$InAs_{0.5}Sb_{0.5}$ T2SLs, revealing the domination of diffusion mechanism. Noteworthily, E_a is determined as 71.12 meV under a bias of −40.5 V, which slightly exceeds half of its bandgap energy (66 meV), indicating that the dark current is primarily dominated by the G-R mechanism. The slightly larger E_a could be attributed to the mall gain and tunneling current at large bias voltage. Through doping control, the depletion region of the device is basically located in the ML, and the G-R dark current of the APD device is suppressed due to the wide bandgap. Since the components of the dark current in APD, such as those arise from band-to-band tunneling and trap-assisted tunneling, are more complicated due to the large bias voltage,[23,51,52] follow-up work requires further analysis to provide design guidance to practical device structure.

Figure 5A shows the current densities and multiplication gain of the APD as a function of bias voltage under 8.4 μm radiation at 100 K. It can be observed that the device's breakdown voltage increases significantly under external radiation because a higher carrier density requires a larger bias voltage to reach saturation. Another key parameter of APD is the breakdown temperature coefficient (C_{bd}), which defines the variation of V_{bd} with temperature. The V_{bd} of an APD tends to rise with increasing temperature due to elevated temperatures leading to heightened phonon scattering, thereby reducing the ionization coefficient.[43,53] When the operating temperature of an APD constructed from materials such as InP or Si fluctuates, the device's gain undergoes significant variations, consequently affecting the device's sensitivity. To determine the C_{bd} of the APD, the device's gain is calculated across various temperatures. Figure 5B illustrates the gain curves of the device spanning temperatures from 100 to 150 K. The voltage when $M = 10$ is extracted as the V_{bd} at the current temperature to calculate C_{bd}. According to the literature,[22] the final calculated C_{bd} of this device is 28.9 mV/K, which is about 450% lower than the structure simulated by Wei-Lin Zhao et al.[54] and is comparable to the mid-wavelength T2SLs APD

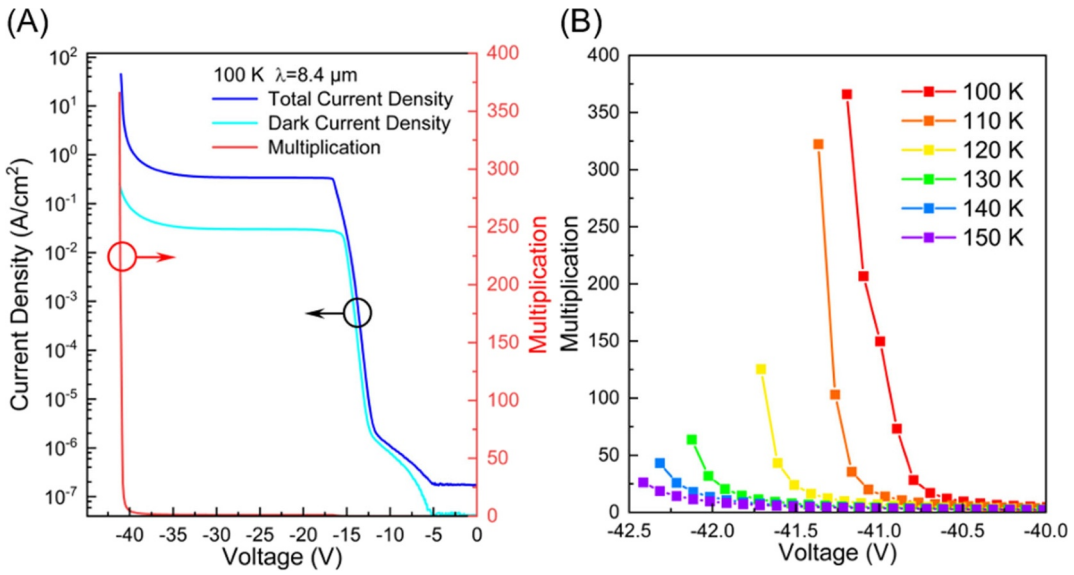

FIGURE 5 (A) The *I-V* curves and gain response of the APD at 100 K. (B) The gain curves at different temperatures. APD, avalanche photodetector.

prepared by Ma et al.[31] A small C_{bd} means that the performance of the device changes less at different temperatures and the device has higher stability. When the temperatures are 110, 120, 130, 140, and 150 K, the gains are 320, 125, 60, 43, and 26, respectively.

Figure 6 shows the spectral response curves of the device at breakdown voltage at different temperatures. It can be seen that the 50% cutoff wavelength of the device is 9.4 μm, which is consistent with the absorption coefficient shown in Figure 1B. Device response decreases as operating temperature increases. At the 100 K and 8.4 μm radiation, the responsivity (R) is calculated to be 650 A/W. The maximum gain of the device at breakdown voltage is finally calculated to be approximately 366. The substantial gain achieved is not only a result of our well-designed device structure but also due to the extremely low k value of the ML. This low k value is attributed to the increased Sb component, which causes the β to further decrease due to the high phonon scattering rate and large hole effective mass.[28]

At this time, the voltage V at unit gain is defined as the voltage value when the second partial differential $\partial^2 I_{ph}/\partial V$ of the photocurrent (I_{ph}) to the voltage is equal to 0.[55] For a device with gain, the relationship between R and QE is given by the formula:

$$R = \frac{\lambda q}{hc}\mathrm{QE}{\cdot}M \tag{2}$$

where h is the Planck constant, c is the speed of light, q is the electron charge, λ is the wavelength of the incident photon, and M is the gain of the device.[56] Then we calculated that at 100 K and 8.4 μm radiation, the QE is 26.28%.

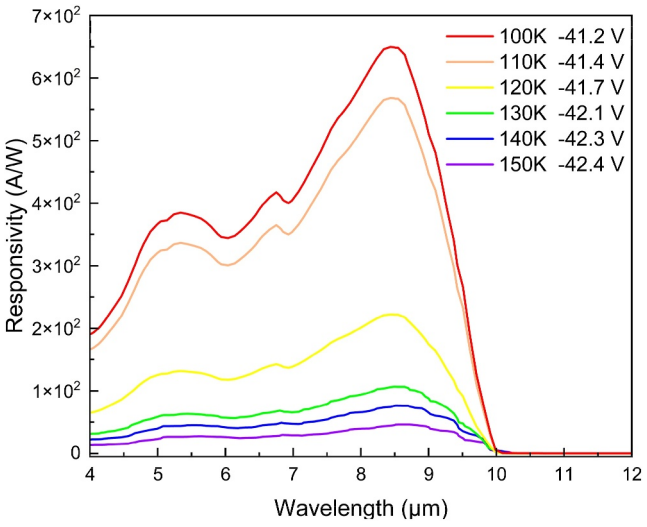

FIGURE 6 Spectral responses R of the device at different temperatures and breakdown voltages.

3 | CONCLUSION

An InAs/InAsSb long-wavelength infrared APD is designed and its device performance is evaluated through simulation. Utilizing a wide-bandgap AlAsSb material with a low k value as the multiplication layer, both tunneling current and G-R current are effectively curtailed, resulting in a dark current density of 5.48×10^{-2} A/cm^2 at 100 K. The gain curves of the device at different temperatures are calculated. At 100 K, the maximum gain of the device reached 366 by using the proposed structure design. Correspondingly, the responsivity reaches 650 A/W, with a QE of 26.28%. In addition, the breakdown

temperature coefficient of this APD is calculated to be 28.9 mV/K indicating favorable temperature stability. By leveraging the unique properties of T2SLs and optimizing the device architecture, this design provides an approach for efficient LWIR detection and potentially high-performance LWIR APDs.

4 | METHODS

Simulations are performed using Crosslight's APSYS software. The band structure is calculated using the zincblende 8 × 8 *k·p* model, in which the envelope function approximation form is adopted. The entire Brillouin zone is assessed. The carrier drift diffusion model was used to calculate the complex carrier dynamics inside the detector, and the impact ionization theory was used as the calculation basis for the APD avalanche gain to ultimately obtain the optoelectronic performance of the device.

ACKNOWLEDGEMENTS

This work was financially supported by the National Natural Science Foundation of China (61974014), the Fundamental Research Funds for the Central Universities (ZYGX2019Z018), and the Innovation Group Project of Sichuan Province (20CXTD0090).

CONFLICT OF INTEREST STATEMENT

The authors declare no conflicts of interest.

ORCID

Jiang Wu https://orcid.org/0000-0003-0679-6196

REFERENCES

1. Haddadi A, Chen G, Chevallier R, Hoang AM, Razeghi M. InAs/InAs$_{1-x}$Sb$_x$ type-II superlattices for high performance long wavelength infrared detection. *Appl Phys Lett*. 2014;105(12):121104. https://doi.org/10.1063/1.4896271
2. Hoang AM, Chen G, Chevallier R, Haddadi A, Razeghi M. High performance photodiodes based on InAs/InAsSb type-II superlattices for very long wavelength infrared detection. *Appl Phys Lett*. 2014;104(25):251105. https://doi.org/10.1063/1.4884947
3. Ting DZ, Khoshakhlagh A, Soibel A, Gunapala SD. Long wavelength InAs/InAsSb infrared superlattice challenges: a theoretical investigation. *J Electron Mater*. 2020;49(11):6936-6945. https://doi.org/10.1007/s11664-020-08349-7
4. Ting DZ, Khoshakhlagh A, Soibel A, et al. Long and very long wavelength InAs/InAsSb superlattice complementary barrier infrared detectors. *J Electron Mater*. 2022;51(9):4666-4674. https://doi.org/10.1007/s11664-022-09561-3
5. Li J, Dehzangi A, Brown G, Razeghi M. Mid-wavelength infrared avalanche photodetector with AlAsSb/GaSb superlattice. *Sci Rep*. 2021;11(1):7104. https://doi.org/10.1038/s41598-021-86566-8
6. Madejczyk P, Gawron W, Sobieski J, Martyniuk P, Rutkowski J. MCT heterostructures for higher operating temperature infrared detectors designed in Poland. *Opto-Electron Rev*. 2023;31:e144551. https://doi.org/10.24425/opelre.2023.144551
7. Cui X, Yuan Q, Guo D, Li C, Shen K, Wu J. Multistep InAs/InAsSb staircase nBn long-wavelength infrared detectors with enhanced charge carrier transport. *Infrared Phys Technol*. 2023;134:104856. https://doi.org/10.1016/j.infrared.2023.104856
8. Ting DZ, Soibel A, Khoshakhlagh A, et al. Complementary barrier infrared detector architecture for long-wavelength infrared InAs/InAsSb type-II superlattice. *Appl Sci*. 2022;12(24):12508. https://doi.org/10.3390/app122412508
9. Gawron W, Kubiszyn Ł Michalczewsk K, Piotrowski J, Martyniuk P. Demonstration of the longwave type-II superlattice InAs/InAsSb cascade photodetector for high operating temperature. *IEEE Electron Device Lett*. 2022;43(9):1487-1490. https://doi.org/10.1109/led.2022.3188909
10. He J, Li Q, Wang P, et al. Design of a bandgap-engineered barrier-blocking HOT HgCdTe long-wavelength infrared avalanche photodiode. *Opt Express*. 2020;28(22):33556-33563. https://doi.org/10.1364/OE.408526
11. Zhu L, Ge H, Guo H, Chen L, Lin C, Chen B. Gain and excess noise in HgCdTe e-avalanche photodiodes at various temperatures and wavelengths. *IEEE Trans Electron Dev*. 2023;70(5):2384-2388. https://doi.org/10.1109/ted.2023.3261820
12. Ciura Ł, Kopytko M, Martyniuk P. Low-frequency noise limitations of InAsSb-, and HgCdTe-based infrared detectors. *Sens Actuators A Phys*. 2020;305:111908. https://doi.org/10.1016/j.sna.2020.111908
13. Yang D, Guo H, Yang L, et al. Characterization of gain and excess noise for mid-wavelength infrared HgCdTe electron avalanche photodiodes. In: Chu J, ed. *Earth and Space: From Infrared to Terahertz (ESIT 2022)*. SPIE; 2023. https://doi.org/10.1117/12.2665331
14. Li Q, Wang F, Wang P, et al. Enhanced performance of HgCdTe midwavelength infrared electron avalanche photodetectors with guard ring designs. *IEEE Trans Electron Dev*. 2020;67(2):542-546. https://doi.org/10.1109/ted.2019.2958105
15. Christol P, Bouschet M, Tornay M, et al. Performance analysis of Ga-free T2SL infrared barrier detector. In: *Infrared Technology and Applications XLIX*. SPIE; 2023;116-126. https://doi.org/10.1117/12.2662892
16. Kim YH, Jung H, Lee HJ, Nah J. HOT MWIR detector development with InAs/InAsSb T2SL nBn structure. In: *2021 International Conference on Electronics, Information, and Communication (ICEIC)*. IEEE; 2021:1-2. https://doi.org/10.1109/ICEIC51217.2021.9369772
17. Ting DZ, Rafol SB, Khoshakhlagh A, et al. InAs/InAsSb type-II strained-layer superlattice infrared photodetectors. *Micromachines*. 2020;11(11):958. https://doi.org/10.3390/mi11110958
18. Christol P, Rodriguez JB. Progress on type-II InAs/GaSb superlattice (T2SL) infrared photodetector: from MWIR to VLWIR spectral domains. In: *International Conference on Space Optics—ICSO 2014*. 2017:694-700. https://doi.org/10.1117/12.2304264
19. Ting DZ, Soibel A, Khoshakhlagh A, et al. InAs/InAsSb superlattice infrared detectors. *Opto-Electron Rev*. 2023;31. https://doi.org/10.24425/opelre.2023.144565
20. Alshahrani DO, Kesaria M, Anyebe EA, Srivastava V, Huffaker DL. Emerging type-II superlattices of InAs/InAsSb and InAs/GaSb for mid-wavelength infrared photodetectors. *Adv Photonics Res*. 2022;3(2):2100094. https://doi.org/10.1002/adpr.202100094
21. Prins AD, Lewis MK, Bushell ZL, Sweeney SJ, Liu S, Zhang YH. Evidence for a defect level above the conduction band edge of InAs/InAsSb type-II superlattices for applications in efficient

infrared photodetectors. *Appl Phys Lett*. 2015;106(17):171111. https://doi.org/10.1063/1.4919549
22. Jin X, Xie S, Liang B, et al. Temperature dependence of the impact ionization coefficients in AlAsSb lattice matched to InP. *IEEE J Sel Top Quant Electron*. 2021;28(2):1-8. https://doi.org/10.1109/JSTQE.2021.3099912
23. Liang Y, Veeramalai CP, Lin G, et al. A review on III–V compound semiconductor short wave infrared avalanche photodiodes. *Nanotechnology*. 2022;33(22):222003. https://doi.org/10.1088/1361-6528/ac5442
24. Campbell JC, Bank SR. Low-noise digital alloy avalanche photodiodes. In: *Advanced Photonics Congress (BGPP, IPR, NP, Networks, NOMA, Sensors, SOF, SPPCom)*. OSA; 2018. https://doi.org/10.1364/IPRSN.2018.IW1B.5
25. Jung H, Lee S, Schwartz M, et al. Growth and characterization of InGaAs/GaAsSb type II superlattice absorbers for 2 μm avalanche photodiodes. *Infrared Technol Appl*. 2022;12107:96-104. https://doi.org/10.1117/12.2622146
26. Kodati SH, Lee S, Guo B, et al. Low noise AlInAsSb avalanche photodiodes on InP substrates for 1.55 μm infrared applications. *Infrared Technol Appl*. 2021;11741:382-389. https://doi.org/10.1117/12.2587884
27. Yi X, Xie S, Liang B, et al. Extremely low excess noise and high sensitivity $AlAs_{0.56}Sb_{0.44}$ avalanche photodiodes. *Nat Photonics*. 2019;13(10):683-686. https://doi.org/10.1038/s41566-019-0477-4
28. Huang J, Zhao C, Nie B, et al. High-performance mid-wavelength InAs avalanche photodiode using $AlAs_{0.13}Sb_{0.87}$ as the multiplication layer. *Photon Res*. 2020;8(5):755-759. https://doi.org/10.1364/PRJ.385177
29. Jin X, Xie S, Liang B, et al. Comparison of the temperature dependence of impact ionization coefficients in AlAsSb, InAlAs, and InP. *Opt Compon Mater*. 2022;11997:63-73. https://doi.org/10.1117/12.2609929
30. Yan S, Huang J, Zhang Y, Ma W. Mid wavelength type II InAs/GaSb superlattice avalanche photodiode with AlAsSb multiplication layer. *IEEE Electron Device Lett*. 2021;42(11):1634-1637. https://doi.org/10.1109/led.2021.3116129
31. Kanedy K, Lopez F, Wood MR, et al. Visualizing period fluctuations in strained-layer superlattices with scanning tunneling microscopy. *Appl Phys Lett*. 2018;112(4):042105. https://doi.org/10.1063/1.5008865
32. Sarney WL, Svensson SP, Yakes MK, Xu Y, Donetsky D, Belenky G. Ultra-short period Ga-free superlattice growth on GaSb. *J Appl Phys*. 2018;124(3):035304. https://doi.org/10.1063/1.5029328
33. Milosavljevic MS, Webster PT, Johnson SR. Impact of unintentional Sb in the tensile InAs layer of strain-balanced type-II InAs/InAsSb superlattices grown on GaSb by molecular beam epitaxy. *J Appl Phys*. 2023;134(5):053103. https://doi.org/10.1063/5.0161046
34. Christol P, Bouschet M, Perez JP, Péré-Laperne N. Barrier structure for Ga-free type-II superlattice midwave infrared photodetector. *Photoptics*. 2023:21-27. https://doi.org/10.5220/0011624500003408
35. Michalczewski K, Tsai TT, Martyniuk P, et al. Higher operating temperature photoresponse of MWIR T2SLs InAs/InAsSb photodetector. In: *13th Conference on Integrated Optics: Sensors, Sensing Structures, and Methods*. SPIE; 2018:217-222. https://doi.org/10.1117/12.2503766
36. Manyk T, Michalczewski K, Murawski K, Martyniuk P, Rutkowski J. InAs/InAsSb strain-balanced superlattices for longwave infrared detectors. *Sensors*. 2019;19(8):1907. https://doi.org/10.3390/s19081907
37. Adachi S. Optical dispersion relations for GaP, GaAs, GaSb, InP, InAs, InSb, $Al_xGa_{1-x}As$, and $in_{1-x}Ga_xAs_yP_{1-y}$. *J Appl Phys*. 1989;66(12):6030-6040. https://doi.org/10.1063/1.343580
38. Höglund L, Ting DZ, Khoshakhlagh A, et al. Influence of radiative and non-radiative recombination on the minority carrier lifetime in midwave infrared InAs/InAsSb superlattices. *Appl Phys Lett*. 2013;103(222):221908. https://doi.org/10.1063/1.4835055
39. Schuler-Sandy T, Myers S, Klein B, et al. Gallium free type II $InAs/InAs_xSb_{1-x}$ superlattice photodetectors. *Appl Phys Lett*. 2012;101(7):071111. https://doi.org/10.1063/1.4745926
40. Steenbergen EH, Connelly BC, Metcalfe GD, et al. Significantly improved minority carrier lifetime observed in a long-wavelength infrared III-V type-II superlattice comprised of InAs/InAsSb. *Appl Phys Lett*. 2011;99(25):251110. https://doi.org/10.1063/1.3671398
41. Jones AH, March SD, Dadey AA, Muhowski AJ, Bank SR, Campbell JC. AlInAsSb separate absorption, charge, and multiplication avalanche photodiodes for mid-infrared detection. *IEEE J Quant Electron*. 2022;58(4):1-6. https://doi.org/10.1109/jqe.2022.3149532
42. Dadey AA, McArthur JA, Kamboj A, Bank SR, Wasserman D, Campbell JC. High-gain low-excess-noise MWIR detection with a 3.5-μm cutoff AlInAsSb-based separate absorption, charge, and multiplication avalanche photodiode. *APL Photonics*. 2023;8(3):036101. https://doi.org/10.1063/5.0136918
43. Huang JJS, Jan YH, Chang HS, et al. Nanoscale III-V semiconductor photodetectors for high-speed optical communications. *Two-Dimens Mater Photodetector*. 2018;3:49-73. https://doi.org/10.5772/intechopen.73054
44. Zhang J, Liu A, Xing H, Yang Y. Study on surface leakage current at sidewall in InP-based avalanche photodiodes with mesa structure. *AIP Adv*. 2022;12(3):035336. https://doi.org/10.1063/5.0080656
45. Ma Y, Zhang Y, Gu Y, et al. Impact of etching on the surface leakage generation in mesa-type InGaAs/InAlAs avalanche photodetectors. *Opt Express*. 2016;24(7):7823-7834. https://doi.org/10.1364/OE.24.007823
46. Woodson ME, Ren M, Maddox SJ, et al. Low-Noise AlInAsSb avalanche photodiode. *Appl Phys Lett*. 2016;108(8):129901. https://doi.org/10.1063/1.4942372
47. Cao P, Peng H, Wang T, et al. Surface passivation of random alloy AlGaAsSb avalanche photodiode. *Electron Lett*. 2023;59(18):e12956. https://doi.org/10.1049/ell2.12956
48. Martyniuk P, Kopytko M, Rogalski A. Barrier infrared detectors. *Opto-Electron Rev*. 2014;22(2):127-146. https://doi.org/10.2478/s11772-014-0187-x
49. Klipstein P. "XB*n*" barrier photodetectors for high sensitivity and high operating temperature infrared sensors. *Infrared Technol Appl*. 2008;6940:935-946. https://doi.org/10.1117/12.778848
50. Deng G, Yang W, Zhao P, Zhang Y. High operating temperature InAsSb-based mid-infrared focal plane array with a band-aligned compound barrier. *Appl Phys Lett*. 2020;116(3):031104. https://doi.org/10.1063/1.5133093
51. Qiu WC, Hu WD, Chen L, et al. Dark current transport and avalanche mechanism in HgCdTe electron-avalanche photodiodes. *IEEE Trans Electron Dev*. 2015;62(6):1926-1931. https://doi.org/10.1109/ted.2015.2417193
52. Li Q, He J, Hu W, Chen L, Chen X, Lu W. Influencing sources for dark current transport and avalanche mechanisms in planar and mesa HgCdTe pin electron-avalanche photodiodes. *IEEE Trans Electron Dev*. 2018;65(2):572-576. https://doi.org/10.1109/ted.2017.2783352
53. Lee S, Jin X, Jung H, et al. High gain, low noise 1550 nm GaAsSb/AlGaAsSb avalanche photodiodes. *Optica*. 2023;10(2):147-154. https://doi.org/10.1364/OPTICA.476963
54. Zhao WL, Wang W, Liu C, et al. Simulation of extended wavelength avalanche photodiode with the type-II superlattice

absorption layer. *Crystals*. 2021;11(10):1210. https://doi.org/10.3390/cryst11101210
55. Meier HTJ. *Design, Characterization and Simulation of Avalanche Photodiodes* [dissertation] Rämistrasse. ETH Zurich; 2011. https://doi.org/10.3929/ethz-a-006445001
56. Lim H, Tsao S, Zhang W, and Razeghi M, High-performance InAs quantum-dot infrared photodetectors grown on InP substrate operating at room temperature. *Appl Phys Lett*. 2007;90(13):131112. https://doi.org/10.1063/1.2719160

How to cite this article: Cheng K, Shen K, Li C, Guo D, Wang H, Wu J. Design of long-wavelength infrared InAs/InAsSb type-II superlattice avalanche photodetector with stepped grading layer. *Electron*. 2024;e73. https://doi.org/10.1002/elt2.73